Strength Contribution by Long-Range Order in Al-containing Refractory High Entropy Alloys

Stephan Laube, Georg Winkens, Alexander Kauffmann*, Juan Li, Christoph Kirchlechner and Martin Heilmaier

Institute for Applied Materials (IAM), Karlsruhe Institute of Technology (KIT), Kaiserstraße 12,
76131 Karlsruhe, Germany

* Corresponding author
mail: alexander.kauffmann@kit.edu (A. Kauffmann)
phone: +49 721 608 42346

Highlights (3 to 5 Bullet points, max. 85 Characters per Bullet point)

- At $T \geq 300$ °C, a strain rate insensitive yield strength was observed in A2 and B2 alloys
- At $T < 300$ °C, the strain rate sensitivity is similar for A2 and B2 alloys
- Solid solution strengthening is low within the (100-x)(MoTiCr)-xAl alloy series
- Ordering is the main contributor to the higher strength of B2 alloys

Abstract (200 / 200 words)

Body-centered cubic refractory high entropy alloys (RHEA) are promising for high-temperature structural application due to their exceptional properties, particularly in terms of yield strength at elevated temperatures. For certain alloy systems, such as Mo-Ti-Cr-Al, both disordered (A2) and ordered (B2) crystal structures are possible. In this particular system, a solid-state transformation from A2 at high to B2 at low temperatures occurs. For Al concentrations above approximately 10 at.%, B2 order is obtained from the transformation temperature down to room temperature, while A2 is stable above room temperature below the critical Al content. In this study, two alloys from the Mo-Ti-Cr-Al system close to the transition between A2 and B2 were investigated. Nanoindentation tests revealed that the magnitude of strain rate sensitivity for both alloys is small compared to classical alloys, however, significantly temperature dependent up to the strength plateau temperatures. The yield strength plateau, which is insensitive to the strain rate, was observed at temperatures exceeding 300 °C. Modelling of solid solution strengthening reproduces the experimental data in the Al-lean A2 alloys. However, the observed discontinuous increase of strength in the Al-rich B2 alloys can only be rationalized by the appearance of B2 order and to no significant other obvious strengthening mechanisms.

Keywords (5 / 5 words)

high entropy alloys (HEA); nanoindentation (NI); mechanical properties; strengthening mechanisms; strain rate sensitivity

1 Introduction

Refractory high entropy alloys (RHEA) are based on the combination of several refractory elements with high melting temperatures, such as W, Mo, Nb, Ta, among others [1]. These alloys exhibit significant potential for use in high-temperature applications. RHEA may also include lighter elements such as Al, Si, and Ti to design alloys of lower density or with improved oxidation resistance [2, 3]. However, many alloy systems are not suitable for commercial use as they exhibit low ductility at room temperature [4]. Apart from secondary intermetallic compounds like Laves phases, which are inherently brittle and might contribute to the brittleness [5, 6], low ductility may be related to the presence of ordered crystal structures [7–11].

Apart from an embrittlement by the presence of order, it might also act as a significant contribution to strength of RHEA which is otherwise governed by solid solution strengthening when being single-phase. The plastic flow in body-centered cubic A2 elemental metals and the strengthening in dilute A2 solid solutions is controlled by screw dislocation motion. However, in A2 RHEA, i.e. concentrated solid solutions with many elements, lattice distortions can be strong enough that edge dislocations might contribute to the alloy strength or even control it [12, 13]. As the screw dislocation motion via kink-pair formation and glide is a thermally assisted process, plastic flow of A2 metals and alloys shows a strong temperature dependency below a critical temperature, the so-called knee temperature (T_{knee}). It can be estimated using the solidus temperature T_{s} as $T_{\mathrm{knee}} \sim 0.25 \cdot T_{\mathrm{s}}$. The process of kink-pair formation is also associated to a strong strain rate sensitivity of the yield strength, since only a limited number of kink pairs can form at a time to accommodate the deformation. Above the knee temperature, kink-pair formation no longer limits dislocation motion, resulting in an almost constant yield strength and no strain rate sensitivity. An additional effect in RHEA is the potentially superimposed strengthening effects due to short-range or long-range atomic order [14], which have been observed in for example the NbTiZr-Al [15] and the NbTiV-Al [16] systems.

The here investigated (100-x_{Al})MoTiCr-x_{Al}Al system [8] also shows the occurrence of order when a threshold of Al content is surpassed. In accordance with FactStage calculations (see Figure 1), a solid-state transformation from A2 at high temperatures to ordered B2 was observed [8, 17], where the constituent elements preferentially occupy the two distinct lattice sites of the B2 unit cell. It is currently not known, which atoms occupy which sites in this system [7]. Furthermore, the actual degree of B2 order is still unknown.

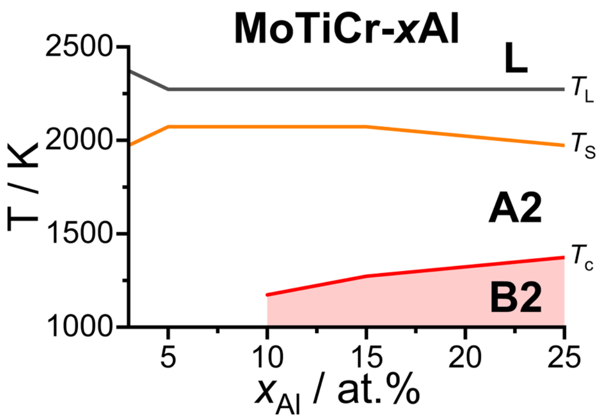

Figure 1: Equilibrium phases as predicted as a function of temperature and concentration of Al x_{Al} for the system (100-x_{Al})MoTiCr-x_{Al}Al by thermodynamic calculations using FactSage and an in-house database. The ratio of Mo, Ti and Cr were kept at equal and the step size of the calculations was 100 K. Data is taken from Ref. [7, 8]. Liquidus (T_{L}, in grey), solidus (T_{S}, in orange) and the order-disorder transition temperature (T_{c}, in red) are highlighted by solid lines.

Similar to the observations in Refs. [4, 18–20], discontinuous plastic deformation occurred during compression testing at elevated temperatures in Ref. [8] for both, A2 and B2 alloys. However, the intensity of stress serrations was significantly different for the two cases and the origin of the discontinuous behavior remained unclear. Apart from this, a distinct strength plateau from 673 K to 1073 K was identified for the A2 alloy. This feature was attributed to a homologous temperature range of 0.32 to $0.52 \cdot T_\mathrm{s}$ and rationalized by similar mobility of edge and screw dislocations at these temperatures [21]. The strength plateau was not undoubtedly determined in case of B2 due to the brittleness of the alloys and the absence of reliable strength data at low temperatures. Based on the calculated solidus temperature (T_s, see Figure 1) and an often used estimate, $0.25 \cdot T_\mathrm{s}$ [21–24], for the knee temperature T_knee as the onset of strength plateau temperature range, the strength plateau is expected at temperatures of $0.25 \cdot T_\mathrm{s}$ ≈ 500 K and above. Apart from a constant strength over a certain temperature range, the above-mentioned microscopic origin related to dislocation mobility also strictly requires a vanishing strain rate dependence of strength [25], which was not verified thus far. Finally, the single-phase A2 alloy exhibited a by 300 MPa lower $R_\mathrm{p0.2}$ as its single-phase B2 counterpart (at 673 K). Possible reasons for this difference might be (i) the order and an associated change in active slip systems or (ii) different amounts of solid solution strengthening.

Based on these findings, two questions are raised: (i) Does the B2 alloy exhibit a yield strength plateau at intermediate temperatures similar to its A2 counterpart. (ii) What is the origin of the significantly higher $R_\mathrm{p0.2}$ of the B2 alloy?

To clarify the origins for the different deformation behavior identified within the (100-x_Al)MoTiCr-x_AlAl system, two compositions were selected to represent alloys with A2 or B2 crystal structure not to close to the critical Al content but still with a rather small difference in Al content: 97(MoTiCr)-3Al (in at%) or 85(MoTiCr)-15Al, respectively. Mo, Ti and Cr were always kept at equal ratios, see Table 1. In the figures throughout this work, blue and green symbols will be used consistently for MoTiCr-3Al and MoTiCr-15Al, respectively. For the reader's convenience the relevant crystal structures will be differentiated by open diamond (A2) and circle (B2) symbols. Since the B2 alloy exhibits brittle failure below 673 K in compression tests [8], nanoindentation at room temperature up to 400 °C was used to characterize the temperature-dependent strength of both alloys. Further, strain rate sensitivity was used to confirm the dislocation mobility related origin of the strength plateau.

2 Experimental and Materials

The investigated samples were synthesized by repetitive arc melting in an Ar atmosphere. The bulk elements Mo (sheet, 99.95%), Cr (granules, 99.5%), Ti (granules, 99.8%) and Al (granules, 99.9%) were provided by chemPur GmbH (Germany). Arc melting was performed within an AM/0.5 furnace supplied by Edmund Bühler GmbH (Germany). To homogenize the microstructure, the samples were annealed under flowing Ar in an HTRH 70-600/18 resistance tube furnace supplied by Carbolite Gero GmbH & Co. KG (Germany). The temperature was set according to the different solidus temperatures to either 1200 °C (MoTiCr-15Al, see Table 1) or 1500 °C (MoTiCr-3Al). The heating rate was 100 K/h, after holding for 20 h the samples were furnace cooled.

The surface of the specimens for microstructural and nanomechanical investigations was first ground with SiC paper up to P2500. A standard metallographic polishing procedure was used with 3 and 1 µm steps, followed by a chemo-mechanical vibratory polishing step utilizing a non-crystallizing oxide polishing suspension with pH = 9.8 (OP-S NonDry, particle size of ~ 40 nm) from Struers GmbH (Germany).

The crystal structure of above mentioned compositions was determined by X-ray diffraction (XRD) with a D2 Phaser from Bruker Corp. (MA, USA) as well as by transmission electron microscopy (TEM), see Ref. [8] for further experimental details. The chemical compositions were analyzed by means of energy-dispersive X-ray spectroscopy (EDS) within a Zeiss EVO50 scanning electron microscope (SEM) from Carl Zeiss AG (Germany). Backscattered electron imaging (BSE) and electron backscatter diffraction (EBSD) were performed utilizing a Zeiss Merlin Gemini II equipped with a Bruker QUANTAX detector. The collected orientation data were evaluated using the software package provided by Bruker. O and N contaminations were determined by using hot carrier gas extraction. The analyzed compositions are presented in Table 1.

Table 1: Determined chemical composition $\bar{x}$ of the investigated alloys by standard-related EDS, given in at%. O and N concentrations were determined by means of carrier gas hot extraction and presented in wt-ppm. O and N are below 860 and 3 at-ppm, respectively.

abbreviation	**heat treatment**	**nominal composition / at%**	**$\bar{x}$ / at%**				**$\bar{x}$ / wt-ppm**	
			Mo	Ti	Cr	Al	O	N
MoTiCr-15Al	1200 °C/20 h	28.33Mo-28.33Cr-28.33Ti-15Al	29.5	27.8	27.7	15.0	231 ± 50	< 0.5
MoTiCr-3Al	1500 °C/20 h	32.33Mo-32.33Cr-32.33Ti-3Al	32.0	32.1	32.7	3.2	134 ± 50	< 0.5

Quasistatic compression tests were performed on a Z100 electro-mechanical universal testing machine supplied by ZwickRoell GmbH & Co. KG (Germany) equipped with a vacuum furnace by Maytec GmbH (Germany). The cuboidal specimens had dimensions of (4 x 3 x 3) mm³ and were extracted from the homogenized samples by means of electrical discharge machining. The initial engineering strain rate $\dot{\varepsilon}$ was set to $10^{-3}\ \mathrm{s}^{-1}$ based on the sample height. Further details on the manufacturing, preparation and characterization steps can be also found in Ref. [8].

Microhardness (mH) was evaluated by using a Q10A+ Vickers hardness tester from ATM Qness GmbH (Germany; formerly Qness GmbH, Austria) with a load of 0.98 N (HV0.1). A minimum number of 16 indents within a random selection of grains were evaluated according to Ref. [26].

Nanoindentation experiments were performed using a Nanoindenter G200 XP supplied by Keysight Technologies, Inc. (CA, USA) with a Berkovich sapphire tip utilizing the continuous stiffness method (CSM). A laser heating stage from Surface systems + technology GmbH & Co. KG (Germany) was employed for high-temperature experiments. The setup heats the indenter tip and the specimen independently to minimize thermal drift effects and it provides a homogeneous temperature distribution [27–29]. The frame stiffness and tip area function were calibrated with fused quartz according to Oliver and Pharr [30, 31]. The dependence of nanohardness (nH) and indentation modulus (E_{Ind}) on temperature was evaluated from room temperature to 400 °C at a constant strain rate (CSR) with $\dot{\varepsilon} \approx 0.5\dot{P}/P = 0.05\ \mathrm{s}^{-1}$ (P is the applied load) up to a maximum indentation depth of 1400 nm. The relation $nH = P/A$ (A is the contact area) was used to calculate the hardness. At each temperature, nH and E_{Ind} were averaged for indentation depths between 1100 and 1300 nm, where nH and E_{Ind} became independent of indentation depth. The calculation of E_{Ind} at each temperature was done according to

$$E_{\mathrm{Ind}} = \frac{(1-\nu^2)\, E_{\mathrm{t}}(T)\, E_{\mathrm{r}}(T)}{E_{\mathrm{t}}(T) - E_{\mathrm{r}}(T)\, (1-\nu_{\mathrm{t}}^2)} \tag{1}$$

where ν is the Poisson's ratio of the specimen, $E_{\mathrm{t}}(T)$ and ν_{t} are Young's modulus and Poisson's ratio of the sapphire tip, respectively [30]. $E_{\mathrm{r}}(T)$ is the measured reduced modulus. The Poisson's ratio for sapphire ($\nu_{\mathrm{i}} = 0.28$) and the examined materials ($\nu = 0.3$) are assumed to be temperature-independent within the investigated temperature regime [29, 30]. The Young's modulus of sapphire is temperature-dependent and was included in the data analysis according to Ref. [32].

Strain rate sensitivity (m) was determined using strain rate jump (SRJ) tests [33], which involved two different strain rates ($\dot{\varepsilon} = 0.05$ and 0.007 s^{-1}) applied sequentially. A constant strain rate of 0.05 s^{-1} was maintained up to the initial 700 nm depth, after which abrupt changes were applied every 200 nm. m can then be calculated using the following formula

$$m = \left(\frac{\partial \ln(\sigma_{\mathrm{f}})}{\partial \ln(\dot{\varepsilon})}\right)_{\varepsilon,T} \approx \left(\frac{\partial \ln(nH/3)}{\partial \ln(\dot{\varepsilon})}\right)_{\varepsilon,T} \quad (2)$$

where the relation between hardness nH and flow stress σ_{f} is approximated with the constraint factor of three [33, 34]. To facilitate comparison, the hardness values obtained at different strain rates at one SRJ test were extrapolated to the identical depth of 1100 nm [35]. The number of successful indentations was greater than eight for both CSR and SRJ tests. Prior to nanoindentation, the deformation-free sample surface was characterized by means of SEM-BSE and EBSD. All of the strain rate jump tests at various temperatures were performed on grains with a surface plane close to $\{110\}$.

3 Results and Discussion

To confirm that a single-phase microstructure was attained after heat treatment, SEM and XRD analyses were performed on both alloys. Figure 2 reveals that the microstructure of both samples is single-phase and homogenous on the micrometer scale. The dendritic microstructure from the as-cast condition is completely removed. The grain size of both alloys is rather large, being several hundred micrometers. As previously discussed in Ref. [8], no additional phases were identified using SEM, TEM and powder XRD, with solely A2-related Bragg peaks being detected.

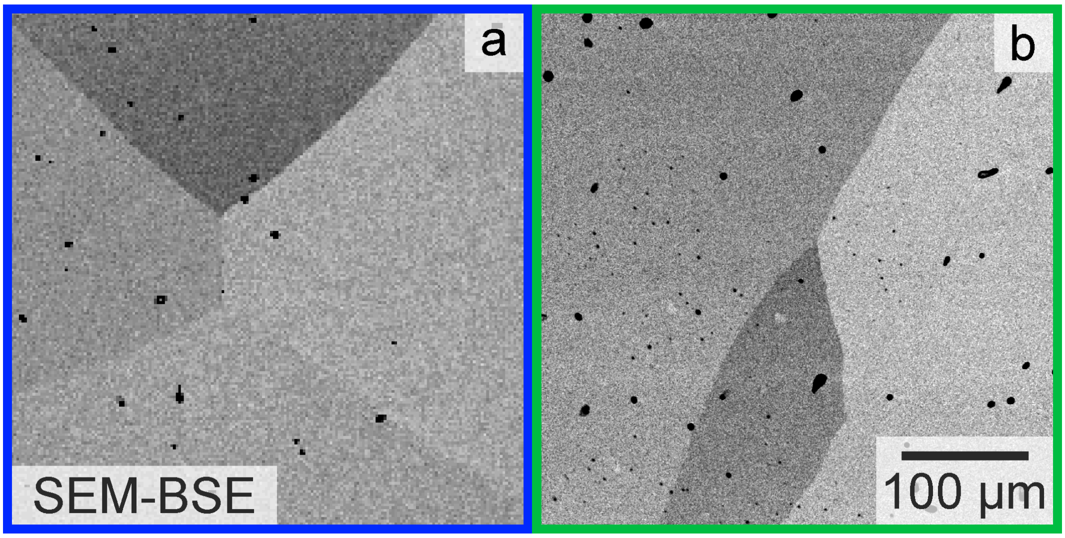

Figure 2: Micrographs of (a) MoTiCr-15Al and (b) MoTiCr-3Al. Pores from casting and homogenization are seen as dark spots. No secondary phases are detected. The grain sizes vary throughout the samples, but the average grain size is always significantly above 100 µm.

In order to evaluate strengthening in the alloys, information about the elastic response is needed. For both alloys, the room temperature indentation modulus E_{Ind} was determined by nanoindentation to be approximately (186 ± 2) and (184 ± 1) GPa for MoTiCr-15Al and MoTiCr-3Al, respectively (see Figure 3). The modulus of both alloys decreases continuously with increasing temperature. For a comparison, Figure 3 includes Young's moduli E for several elements, being constituents of the present alloys (including Ta) and the experimentally determined indentation moduli. The respective crystal structures are given by their *Strukturbericht* designation. The two investigated alloys have similar indentation moduli and exhibit also a similar trend with temperature compared to the displayed Young's moduli. At room temperature, both alloys have similar moduli compared to pure Ta [36] and other RHEA from the Mo-Nb-Ta-V, Mo-Ta-Zr and Al-Mo-Ta-Ti-V systems [37] (not shown here).

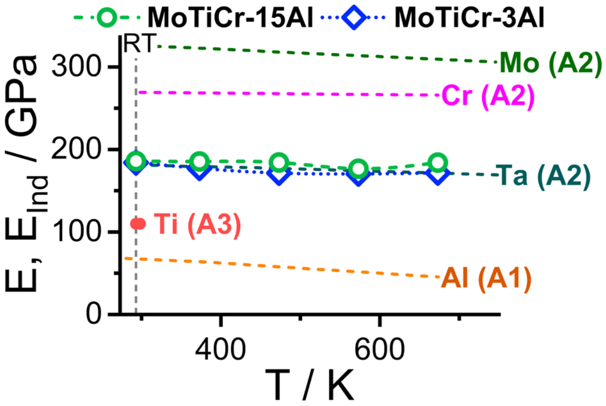

Figure 3: Young's moduli E and Indentation moduli E_{Ind} as a function of temperature (T). The data for the pure elements are extracted from Ref. [36] for Ta, Mo and Al; Ref. [38] for Ti and Ref. [28] for Cr. Indentation moduli of both alloys are within the expected range and slope for the Young's moduli of refractory metal-based alloys.

Due to the macroscopic brittleness of MoTiCr-15Al, no evaluation of the macroscopic strength of this alloy is possible below 673 K [8]. Therefore, nanohardness tests were conducted at temperatures between RT and 673 K. The hardness of both alloys was determined at three different strain rates, and Figure 4 displays the experimental results. A nH^{RT} of (7.3 ± 0.1) and (8.9 ± 0.1) GPa for MoTiCr-15Al and MoTiCr-3Al, respectively, was found for the lowest strain rate. The hardness decreases with increasing temperature, leading to a $nH^{673\text{ K}}$ of (5.5 ± 0.6) and (7.6 ± 0.4) GPa for MoTiCr-15Al and MoTiCr-3Al, respectively.

As can be seen in Figure 4, MoTiCr-15Al displays a higher nH than the disordered MoTiCr-3Al at all test temperatures. A decrease in strain rate to $0.001\ \text{s}^{-1}$ results in a drop of approximately four to five percent in nH^{RT} for both alloys (see the inset in Figure 4). As the change in nH with temperature and the error from the experimental testing overlap, the strain rate sensitivity has to be evaluated in order to confirm the appearance of athermal strength plateau expected based on dislocation mobility arguments for metals and alloys with A2 crystal structures and superstructures thereof [25].

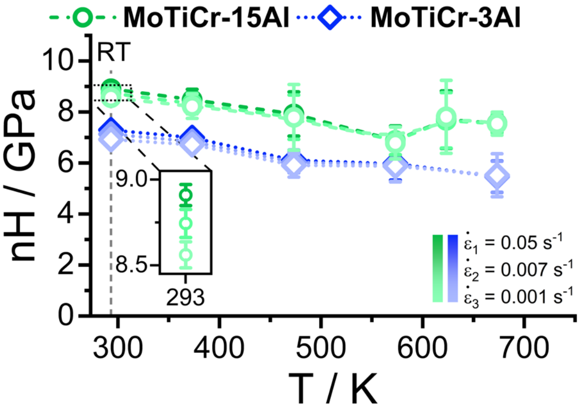

Figure 4: Hardness (nH) determined by nanoindenation at various temperatures (T) and deformation rates ($\dot{\varepsilon} = 0.5\dot{P}/P$). The hardness of both alloys decreases with increasing temperature.

The strain rate sensitivity m was determined for each alloy and is depicted in Figure 5, together with literature data from a selection of other refractory metals. In contrast to Cr, Mo and Ta, both alloys show a rather low m value of $m^{\mathrm{RT}} \approx 0.01$ at ambient temperature. m^{RT} was obtained for Cr by nanoindentation to be in the range from 0.023 to 0.07, depending on the grain size [28, 39, 40]. Similarly, a range of 0.025 to 0.06 was determined for Ta in tensile testing for different grain sizes [43]. For Mo, m^{RT} was determined to be 0.024 from nanoindentation experiments, while macroscopic compression testing revealed an m^{RT} of 0.042 [41, 42]. Additionally, the measured value for the strain rate sensitivity can also depend on the tested range of strain rates [43] or the purity of the metal [44]. Therefore, only a qualitative assessment of measuring either a finite or vanishing strain rate sensitivity is used here. As the temperature increases, both alloys show a similar trend. An almost constant finite m from ambient temperature to 473 K is obtained, followed by a sharp drop to almost zero at 573 K, succeeded by a plateau with m approaching zero until 673 K. Hence, the knee temperature T_{knee} as the onset temperature of the temperature-insensitive strength regime for both alloys ($T_{\mathrm{s}} \approx (1973 - 2073)$ K [8]) is in the range of $T_{\mathrm{knee}} = (573 - 673)$ K. This is a plausible range when compared to Cr with $T_{\mathrm{s}} \approx$ 2134 K [45, 46] and $T_{\mathrm{knee}} \approx (650\ -\ 670)$ K [44]. The appearance of an athermal strength plateau at temperatures of 673 K and higher for both alloys is confirmed [8].

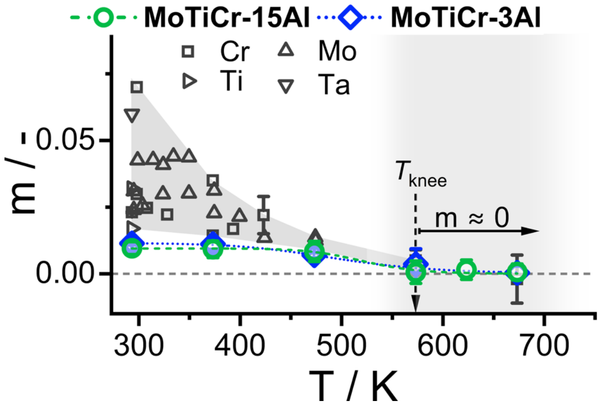

Figure 5: Strain rate sensitivity (m) as a function of temperature (T) for MoTiCr-15Al, MoTiCr-3Al and various refractory metals. Data for Cr from Ref. [28, 39, 40], Ta from Ref. [47], Mo from Ref. [41, 42] and Ti from Ref. [48]. For both alloys, the magnitude of m^{RT} is small at ambient temperature compared to pure Cr, Mo and Ta. Above 473 K, a steep drop of m is determined and above 573 K, m is approximately zero. Similar behavior is reported for pure refractory metals, which approach their T_{knee} at a comparable temperature.

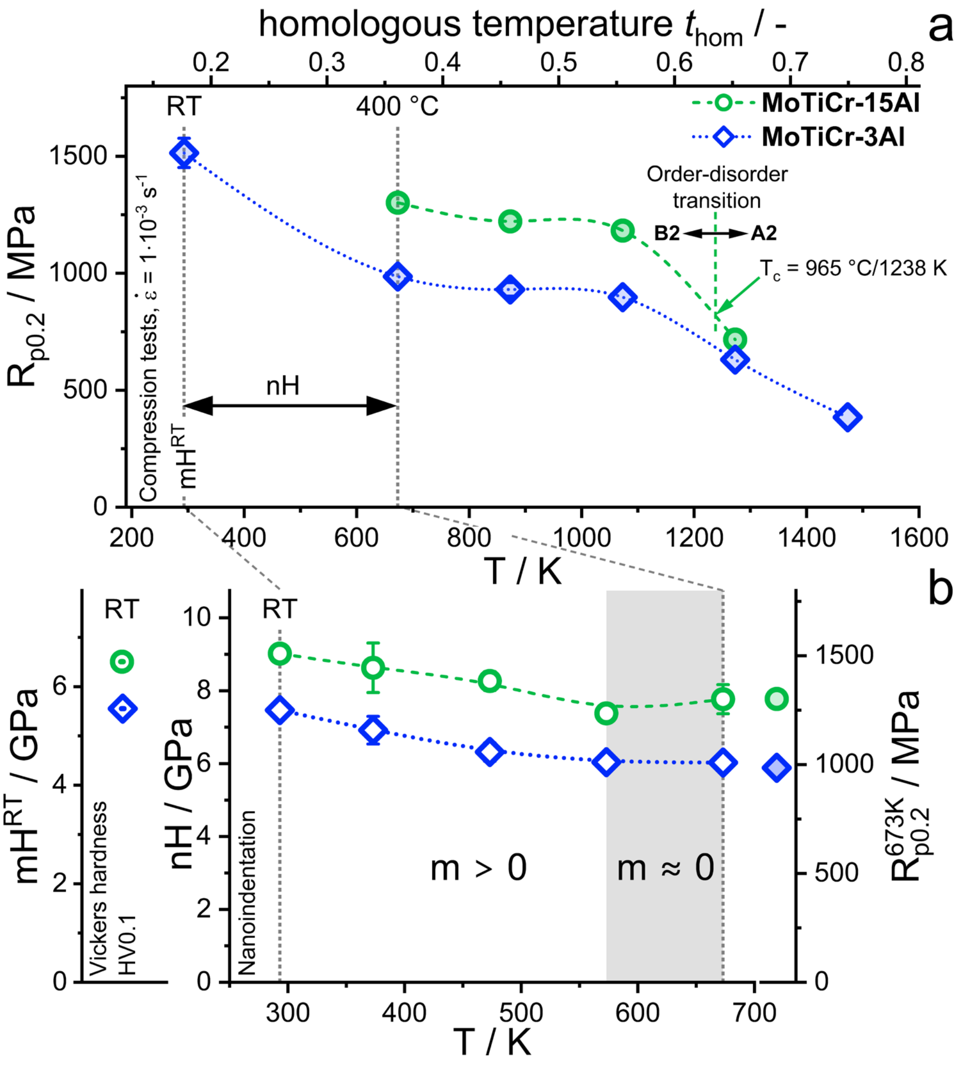

Figure 6: (a) Yield strength ($R_{p0.2}$) as a function of temperature as determined by means of compression tests. Part of the data is taken from Ref. [8]. (b) The temperature-dependent nanoindentation (right, nH) and Vickers microhardness test (left, mH^{RT}) results are presented for both alloys, with scale bars fitted for a visual comparison. The analysis indicates that MoTiCr-15Al exhibits superior yield strength and hardness, compared to MoTiCr-3Al.

In order to assess the validity of nanoindentation testing on a macroscopic scale, Vickers microhardness (mH) and compression test results were carried out and included in Figure 6. Figure 6a shows that only for the MoTiCr-3Al alloy, a reasonable $R_{p0.2}$ value at RT was determined as a result of brittle failure of MoTiCr-15Al before yielding. In the temperature range tested, the B2-ordered, Al-rich alloy exhibits higher yield strength compared to the Al-lean, A2 alloy. For both alloys, yield strength remained at a similar value between temperatures ranging from 673 to 1073 K, with significant decreases observed for temperatures beyond 1073 K due to the onset of diffusion-controlled creep deformation even at quasi-static strain rates. The comparatively large change in yield strength between 1073 K and 1273 K in case from MoTiCr-15Al might be additionally related to the transition from the B2 ordered to the A2 disordered crystal structure at the transition temperature (T_c). This phase transition at $T_c \approx 1238$ K was previously assessed by complementary differential scanning calorimetry (DSC) and thermodynamic calculations (see Figure 1 and Ref. [8]).

For the Vickers microhardness tests, the potential influence of grain boundary strengthening can be neglected as the indentation close to grain boundaries was avoided. As shown in Figure 6b, mH at ambient temperature can be approximately correlated to nH. At 673 K, nH correlated well with yield strength, as illustrated in Figure 6b on the right side. Thus, it appears that single-grain nanoindentation can be scaled to macroscopic testing by correction factors, being $mH^{\mathrm{RT}}/\mathrm{GPa} \approx 0.71 \cdot nH^{\mathrm{RT}}/\mathrm{GPa}$ and $R_{\mathrm{p0.2}}^{673\,\mathrm{K}}/\mathrm{MPa} \approx 166 \cdot nH^{673\,\mathrm{K}}/\mathrm{GPa}$. This observation leads to the conclusion, that several factors impacting the mechanical properties are comparable in magnitude in both compositions, for example orientation-dependency of hardness, work hardening between 0.2 and approx. 8 % plastic strain [34], or decrease in hardness as a function of indentation depth, i.e. the indentation size effect.

As previously stated, the B2-ordered alloy MoTiCr-15Al exhibits a higher yield strength at ambient and elevated temperatures compared to its A2 counterpart MoTiCr-3Al, irrespective of the length scale of deformation. However, despite the similar trend in strain rate sensitivity and comparable knee temperature, a thorough investigation of the various strength contributions is necessary due to the compositional difference and the unclear degree of B2 order [49–52].

The potential key factors influencing the strength and deformation behavior of these alloys might be the following: (i) Grain size as governed by the Hall-Petch relationship: The grain size was found to be similar and large for both alloys. Therefore, it can be considered negligible here. (ii) Dislocation density: it is assumed to be low and similar in both starting conditions, because both alloys were homogenized at relatively high homologous temperatures and cooled slowly within the furnace. (iii) Secondary phases (causing particle strengthening) are not present in either case (see Ref. [8] for details). (iv) The evaluation of orientation strengthening can be omitted, since only orientations with surface planes close to {110} were tested in the nanoindentation experiments and, as mentioned before, the orientation strengthening seems to be similar in both alloys, as can be estimated from the following ratios:

$$\frac{nH_{\mathrm{MoTiCr-3Al}}^{637\,\mathrm{K}}}{nH_{\mathrm{MoTiCr-15Al}}^{637\,\mathrm{K}}} \approx \frac{R_{\mathrm{p0.2,MoTiCr-3Al}}^{637\,\mathrm{K}}}{R_{\mathrm{p0.2,MoTiCr-15Al}}^{637\,\mathrm{K}}} \tag{3}$$

(v) The potentially different, temperature-dependent strength contribution (below the knee temperature) is irrelevant as the alloys were evaluated exclusively above their respective knee temperatures in the athermal strength regime. (vi) The deformation rate does not have a significant impact at temperatures above the knee temperature and below the diffusion-controlled temperature regime. (vii) The strengthening by interstitial elements, such as O or N, is expected to be similar since the contamination with those impurities is on a comparable level (see Table 1).

Excluding the above-mentioned contributions to strength, only solid solution strengthening and order strengthening remain as possible reasons for the observed difference in strength between the A2 and B2 alloys. Solid solution strengthening is a crucial factor as the composition between the two alloys is different, and it will be discussed subsequently. The recent analytical models for screw and edge dislocation-controlled strengthening in HEA by Maresca and Curtin will be used. As the strength-controlling dislocation type is not known for (100-*x*)MoCrTi-*x*Al solid solutions, strengthening will be modelled using both dislocation types. Detailed information on the implementation of screw and edge dislocation-controlled strengthening models has been described previously for example in Refs. [53–55], and only the key points for the application are described here.

To evaluate the edge dislocation-controlled strengthening (without any free parameter), only readily available, experimental input parameters of the alloys and their constituent elements are required. These include the length of the Burgers vector $\bar{b}$ (and hence the lattice parameter $\bar{a}$) of the alloy, the alloy's shear modulus $\bar{G}$ and Poisson's ratio $\bar{\nu}$. The numerical factor α is set to $1/8$ to evaluate the dislocation line tension with $\Gamma = \alpha\, \bar{G}\, \bar{b}^2$. The zero Kelvin yield strength τ_{y0} and energy barrier for edge dislocation-controlled strength are calculated via:

$$\tau_{y0} = 0.04\,\alpha^{-1/3}\,\bar{G}\left(\frac{1+\bar{\nu}}{1-\bar{\nu}}\right)^{4/3}\left[\frac{\sum_n x_n\,\Delta V_n^2}{\bar{b}^6}\right]^{2/3} \tag{4}$$

$$\Delta E_\mathrm{b} = 2.00\,\alpha^{1/3}\,\bar{G}\,\bar{b}^3\left(\frac{1+\bar{\nu}}{1-\bar{\nu}}\right)^{2/3}\left[\frac{\sum_n x_n\,\Delta V_n^2}{\bar{b}^6}\right]^{1/3} \tag{5}$$

ΔV_n, the misfit volume for each constituent element n, is weighted by the respective concentration x_n. It is calculated as the difference between the atomic volume of each element and the resulting alloy in the multicomponent system with $\Delta V_n = V_n - V_\mathrm{alloy}$ (see e.g. Ref. [13]).

The commonly used calculation scheme using concentration-weighted single crystal stiffnesses (e.g. Refs. [13, 53, 54, 56]) did not agree with the experimental results ($\bar{E}_\mathrm{model} = 233$ GPa as compared to $\bar{E}_\mathrm{Ind} = 186$ GPa for MoTiCr-3Al, for example). Thus, the experimentally obtained indentation modulus was used. Using a Poisson's ratio of $\bar{\nu} = 0.3$, a concentration independent $\bar{G} = 71$ GPa was then used for the modelling.

The temperature-dependent yield strength can then be calculated with the following equation:

$$\sigma_\mathrm{y}(T,\dot{\varepsilon}) = 3.06\,\tau_{y0}\exp\left[-\frac{1}{0.55}\left(\frac{k_\mathrm{B}\,T\ln(\dot{\varepsilon}_0/\dot{\varepsilon})}{\Delta E_\mathrm{b}}\right)^{0.91}\right] \tag{6}$$

With a reference strain rate of $\dot{\varepsilon}_0 = 10^4\ \mathrm{s}^{-1}$ and experimental one of $\dot{\varepsilon} = 10^{-3}\ \mathrm{s}^{-1}$. The thermal energy is calculated with the Boltzmann constant k_B. The Taylor factor 3.06 is used here for edge dislocation slip in polycrystalline A2 materials on $\{110\}\langle 1\bar{1}1\rangle$ slip systems, according to Ref. [57].

The method described by Chen et al. [58] was used to optimize the atomic radii r of the individual elements in Mo-Cr-Ti-Al. For a relevant database, values for Nb-containing alloys were also included in the refinement process. Part of the data is presented in Figure 7. As expected, the atomic radii in an A2 solid solution are significantly different for elements with A1 and A3 crystal structures at ambient temperature. The lattice parameter, as a concentration-weighted average of the optimized elemental values of the A2 or B2 alloys, reproduces the experimental data reasonably well.

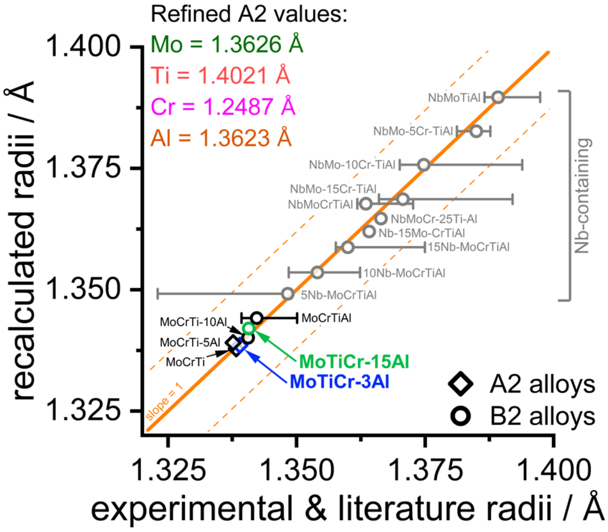

Figure 7: Assessment of experimental & literature vs. refined/recalculated atomic radii r for different alloys. Data is taken from Ref. [8, 58]. Literature data for the elements Al, Ti, Nb, Mo and Cr is taken from Ref. [59]. A2 Ti is extrapolated from high temperature to RT by considering the coefficient of thermal expansion [60]. The solid line represents a slope of one, thus indicating no change from experimental values to refined values. The two dotted lines indicate a five percent error band. Individual error bars smaller than the symbol size are omitted.

The individual lattice parameters of the (100-x)MoTiCr-xAl alloys are depicted in Figure 8. The lattice parameters increase with increasing Al concentration, starting from a_{MoTiCr} = 3.09 Å at zero Al and reaching a_{MoTiCrAl} = 3.099 Å at the equimolar concentration [8, 58]. As displayed by the solid orange line, the concentration weighted values of the elemental lattice parameters [61] provide a reasonably good fit to the experimental data.

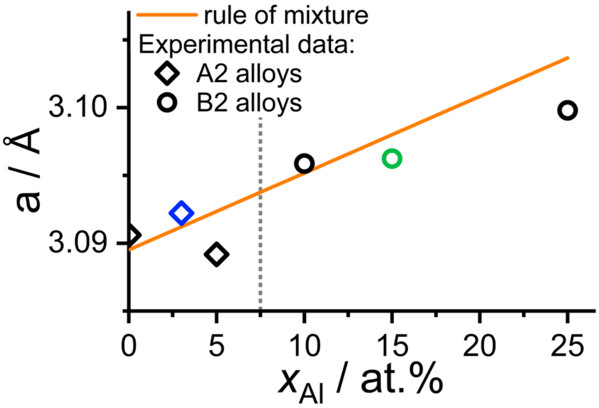

Figure 8: Determined lattice parameters a by XRD using the weighted function similar to that proposed by Nelson-Riley [62]. Based on the refined atomic radii, the lattice parameters for varying Al concentrations are calculated according to the linear rule of mixture [61] (solid line). A small deviation to the linear trend is observed at higher Al concentrations. Raw data is taken from Refs. [8, 58].

The strength predicted by the edge dislocation model is depicted in Figure 9, together with the experimental $R_{\mathrm{p0.2}}$ at 673 K for the previously presented compositions from the (100-x)MoTiCr-xAl system. While the absolute magnitude of the predicted strength is well reproduced, the concentration-dependent trend is not properly captured. The modelled strength decreases with increasing Al content, because the concentration of Cr decreases, the element which causes the largest volume misfit due to its small lattice parameter. However, the A2 alloys show a slight increase in strength over the concentration range. The largest deviation is found for the Al-free alloy with a predicted value of 1100 MPa compared to the measured 965 MPa. However, for MoTiCr-5Al, the modelled value of 1055 MPa is only 10 MPa larger than the experimental one.

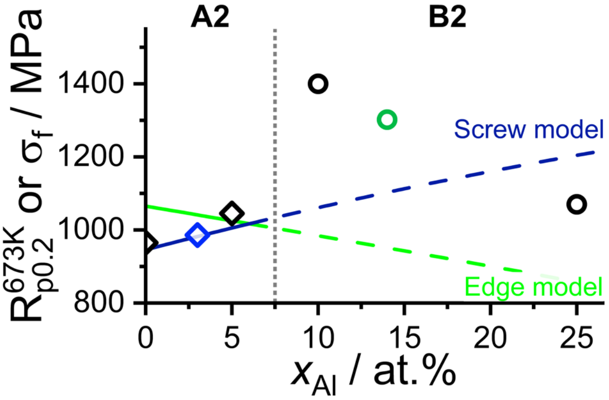

Figure 9: $R_{\mathrm{p0.2}}^{673\mathrm{K}}$ and the calculated flow stress σ_{f} of the edge and screw model (in solid lines). The fitted screw model (in blue) [56] predicts the strength of the A2 alloys well while failing to reproduce the trend of the B2 alloys. However, the edge model (in green) [63] captures the trend of the B2 alloys reasonably but does not represent the trend of the A2 alloys.

The strength predicted by the screw dislocation model is also shown in Figure 9. Yield strength contributions by kink glide, τ_{k} and cross-kink breaking, τ_{xk} were considered for screw dislocation motion. For a detailed discussion of the screw dislocation model, the reader is referred to Ref. [55]. τ_xk can be calculated using:

$$\tau_\mathrm{xk}(T,\dot{\varepsilon}) = \frac{\pi\,\bar{E}_\mathrm{i}}{\bar{a}_\mathrm{p}\,\bar{b}\,\zeta_\mathrm{i}}\left[1-\left(\frac{\Delta H}{\bar{E}_\mathrm{i}}\right)^{2/3}\right] \tag{7}$$

where the energy for self-interstitial formation $\bar{E}_\mathrm{i}$ and a characteristic length scale ζ_i determine this strength contribution. $\bar{a}_\mathrm{p}$ denotes the distance of low-potential valleys. The enthalpy barrier $\Delta H = k_\mathrm{B} \cdot T \cdot \ln(\dot{\varepsilon}_0/\dot{\varepsilon})$ captures experimental parameters.

For kinks to glide along the dislocation, a stress τ_k is required:

$$\tau_\mathrm{k}(T,\dot{\varepsilon}) = \tau_\mathrm{b} + \tau_\mathrm{c}\left[3.26\left(\frac{\Delta H}{\Delta\tilde{E}_\mathrm{p}} - 0.06\frac{\bar{E}_\mathrm{k}}{\Delta\tilde{E}_\mathrm{p}} + 1.07\sqrt{\frac{\bar{w}_\mathrm{k}}{\bar{b}}}\right)^{-1} - 1.58\frac{\Delta\tilde{E}_\mathrm{p}}{\bar{E}_\mathrm{k}}\right] \tag{8}$$

where τ_b and τ_c are characteristic stresses describing the glide process. $\bar{w}_\mathrm{k}$ is the kink width, approximately $10\,\bar{b}$, and $\bar{E}_\mathrm{k}$ is the kink formation energy. $\Delta\tilde{E}_\mathrm{p}$ quantifies the change in local potential environment due to kink glide. Its precise value can only be obtained by first principles; thus, a fitting procedure will be discussed below to obtain plausible values.

The macroscopic stress for plastic deformation of the alloy is then determined by the stresses for the two processes described, the cross-kink breaking and the kink glide. The Taylor factor is set as 2.74 for screw dislocation slip by pencil glide in disordered A2 polycrystals [51]. This dislocation slip occurs along $\langle 111\rangle$ directions, with several sets of slip planes contributing to the resulting formula:

$$\sigma_\mathrm{y}(T,\dot{\varepsilon}) = 2.74\left(\tau_\mathrm{xk}(T,\dot{\varepsilon}) + \tau_\mathrm{k}(T,\dot{\varepsilon})\right) \tag{9}$$

$\bar{a}_\mathrm{p}$ and $\bar{b}$ are obtained from the concentration weighted, optimized lattice parameters of the constituent elements. The self-interstitial energy $\bar{E}_\mathrm{i}$ is calculated as the concentration-weighted average of elemental data from first-principles simulations (see Refs. [64–66] for details). $\bar{E}_\mathrm{k}$ was calculated as a concentration-weighted average of the elements [67, 68]. For Ti with A2 crystal structure, $2E_\mathrm{k} = 1$ eV was used, see also the approach for the binary Mo-Ti system in Ref. [54]. For Al, the mean value of the other elements was used, as to the best of the authors' knowledge, no literature data is available.

To approximate $\Delta\tilde{E}_\mathrm{p}$, the method from Ref. [54] was adapted, where a fitting procedure was used: assuming concentration-weighted energy contributions ΔU of all constituent elements n, $\Delta\tilde{E}_\mathrm{p}$ can be calculated via [53, 55]:

$$\Delta\tilde{E}_\mathrm{p} = \sqrt{\sum_{n=\mathrm{Mo,Cr,Ti,Al}} x_n\,\Delta U_n^2} = \sqrt{x_\mathrm{Al}\,\Delta U_\mathrm{Al}^2 + \underbrace{x_\mathrm{Mo}\,\Delta U_\mathrm{Mo}^2 + x_\mathrm{Cr}\,\Delta U_\mathrm{Cr}^2 + x_\mathrm{Ti}\,\Delta U_\mathrm{Ti}^2}_{x_\mathrm{MoTiCr}\,\Delta U_\mathrm{MoTiCr}^2}} \tag{10}$$

Since Mo, Cr and Ti are always present in equal proportions, their impact cannot be further distinguished and their individual contributions are combined into a single variable. The value of ΔU_MoTiCr was determined by fitting σ_y to the experimental result of the equimolar MoTiCr. Here, $\Delta U = \Delta\tilde{E}_\mathrm{p}(x_\mathrm{Al} = 0) = 97$ meV was obtained. This value is plausible when compared to fitted values for other multicomponent systems, ranging from 67 to 108 meV [53].

The free parameter ΔU_Al was then fitted to the experimental data from MoTiCr-3Al and MoTiCr-5Al, yielding $\Delta U_\mathrm{Al} = 169$ meV. Values for ΔU were reported in Refs. [53, 55] as between 137 and 194 meV for different solute-matrix combinations, thus the value for ΔU_Al also is plausible. The overall impact of these small Al contents on $\Delta\tilde{E}_{\mathrm{p}}$ is, however, small. The respective values of $\Delta\tilde{E}_{\mathrm{p}} = 100$ and $102\ \mathrm{meV}$ are still well within the range of literature values [53].

As the values for the two free parameters in the screw dislocation model, ΔU_{Al} and $\Delta U_{\mathrm{MoTiCr}}$, were obtained by fitting to the experimental data, modelling and experimental results are in good agreement for the A2 alloys, see Figure 9. A fit to room temperature data of the A2 alloys yielded similar results for $\Delta U_{\mathrm{MoTiCr}}$ and ΔU_{Al}, with 94 and $187\ \mathrm{meV}$, respectively (not shown here). As these values are temperature-independent, the similar results further support the values presented here. However, obtained energy values can only be conclusively confirmed with DFT simulations of this specific alloy system.

Extrapolating the model predictions from the A2 alloys to the B2 alloys, the screw dislocation model does *not* capture the yield strengths in the latter. Neither the jump nor the decrease in strength for larger Al contents can be explained by the current model. If there is screw dislocation controlled strengthening in the ordered alloys, additional energy contributions need to be considered to account for the observed course and magnitude in strength. This missing link likely depends on properties specific to ordered materials, like the anti-phase boundary energy and/or the degree of order.

The failure of the edge dislocation model to capture the trend in A2 alloys with increasing Al concentration is likely caused by the simplified assumptions in the modeling, namely the linear change in lattice parameter and the concentration-independent shear modulus. However, it predicts the absolute values of yield strength well for the A2 alloys, without the need for fitting of any parameters. Instead, only the experimentally available indentation modulus and lattice parameter data are used, which were obtained by independent analyses. In Ref. [53], a transition from screw to edge dislocation-controlled strength was proposed, when a threshold value of the misfit $\delta = \frac{1}{3V_{\mathrm{alloy}}}\left(\sum_n x_n\, \Delta V_n^2\right)^{0.5}$ of $\delta_{\mathrm{th}} = 0.035$ is surpassed. All alloys investigated here surpass this threshold, their misfits range from $\delta_{0\mathrm{Al}} = 0.048$ for MoTiCr to $\delta_{25\mathrm{Al}} = 0.041$ for MoTiCr-25Al. Thus all alloys are likely edge dislocation-controlled according to Ref. [53]. However, also this model does not capture the strength of the B2 alloys. While the trend with increasing Al content is similar in the edge dislocation model and the experimental strength of B2 alloys, the model strength is ≈ 400 MPa smaller than the experimental values.

Thus, neither model for solid solution strengthening predicts the increase in strength observed between A2 and B2 alloys, leading to order strengthening as the only remaining phenomenon to explain the results.

4 Conclusions

1. In single-phase A2 and B2 (100-*x*)(MoTiCr)-*x*Al alloys, the strength plateau with vanishing strain rate sensitivity was verified and knee temperatures are between 573 K and 673 K.
2. At the plateau temperature, the B2 alloy exhibits a higher strength (examined on multiple length scales) by ~ 300 MPa as compared to its A2 counterpart. Relevant potential factors causing the strength difference between A2 and B2 such as different elastic constants, different homologous temperatures, secondary phases and grain size are ruled out as determining; the much higher strength of B2 is primarily related to the order.
3. Modeling of solid solution strengthening using the Maresca-Curtin models [53, 56, 63] is successful for the A2 alloys from the (100-*x*)(MoTiCr)-*x*Al alloy series. In contrast to earlier model implementations [13, 53, 54, 63], elastic moduli cannot be calculated from the concentration weighted single crystal stiffnesses of the individual elements in these alloys and need to be experimentally determined.
4. Neither of the models captures the large increase of strength of the B2 ordered alloys correctly, as peculiarities of the dislocation behavior in ordered alloys are not included in the models. This

is opposed to the findings in ordered FCC NiCoCr, where no effect of ordering was observed [69].

Acknowledgments

This work was supported by the Deutsche Forschungsgemeinschaft (DFG), grant no. HE 1872/34-2 and by the "Future Fields" project "ACDC" of the strategy of excellence of the Karlsruhe Institute of Technology (KIT). GW and MH are thankful to the DFG for funding under the umbrella of the research training group RTG 2561 "MatCom-ComMat: Materials Compounds from Composite Materials for Applications in Extreme Conditions". CK and JL acknowledge financial support by the Robert-Bosch-Foundation and the Helmholtz Program "Materials Systems Engineering: Functionality by Design". The chemical analysis by ICP-OES at the Institute for Applied Materials (IAM-AWP), Karlsruhe Institute of Technology (KIT) is gratefully acknowledged.

Data Availability Statement

The data presented in this study are available in KITopen at https://doi.org/10.35097/1784 under CC BY-SA 4.0 license. Further information is available upon request with alexander.kauffmann@kit.edu.

References

[1] S. GORSSE *et al.: From high-entropy alloys to complex concentrated alloys*, Comptes Rendus Physique 19 (2018), p. 721 – 736.

[2] B. GORR *et al.: A new strategy to intrinsically protect refractory metal based alloys at ultra high temperatures*, Corrosion Science 166 (2020), No. 108475.

[3] S. GORSSE *et al.: Mapping the world of complex concentrated alloys*, Acta Materialia 135 (2017), p. 177 – 187.

[4] H. CHEN *et al.: Microstructure and mechanical properties at elevated temperatures of a new Al-containing refractory high-entropy alloy Nb-Mo-Cr-Ti-Al*, Journal of Alloys and Compounds 661 (2016), p. 206 – 215.

[5] F. MÜLLER *et al.: Formation of complex intermetallic phases in novel refractory high-entropy alloys NbMoCrTiAl and TaMoCrTiAl: Thermodynamic assessment and experimental validation*, Journal of Alloys and Compounds 842 (2020), No. 155726.

[6] F. STEIN; Leineweber, Andreas: *Laves phases: a review of their functional and structural applications and an improved fundamental understanding of stability and properties*, Journal of Materials Science 56 (2021), p. 5321 – 5427.

[7] H. CHEN *et al.: Crystallographic ordering in a series of Al-containing refractory high entropy alloys Ta–Nb–Mo–Cr–Ti–Al*, Acta Materialia 176 (2019), p. 123 – 133.

[8] S. LAUBE *et al.: Controlling crystallographic ordering in Mo–Cr–Ti–Al high entropy alloys to enhance ductility*, Journal of Alloys and Compounds 823 (2020), No. 153805.

[9] R. SCHROLL *et al.: Core properties and motion of dislocations in NiAl*, Acta Materialia 46 (1998), p. 903 – 918.

[10] T. M. POLLOCK *et al.: A comparative analysis of low temperature deformation in B2 aluminides*, Materials Science and Engineering: A 317 (2001), p. 241 – 248.

[11] C. T. LIU *et al.: Recent advances in B2 iron aluminide alloys: deformation, fracture and alloy design*, Materials Science and Engineering: A 258 (1998), p. 84 – 98.

[12] C. R. WEINBERGER *et al.: Slip planes in bcc transition metals*, International Materials Reviews 58 (2013), p. 296 – 314.

[13] C. LEE *et al.: Strength can be controlled by edge dislocations in refractory high-entropy alloys*, Nature communications, No. 5474.

[14] K. DAS; Das, S.: *Order-disorder transformation of the body centered cubic phase in the Ti-Al-X (X = Ta, Nb, or Mo) system*, Journal of Materials Science 38 (2003), p. 3995 – 4002.

[15] N. YURCHENKO *et al.: Overcoming the strength-ductility trade-off in refractory medium-entropy alloys via controlled B2 ordering*, Materials Research Letters 10 (2022), p. 813 – 823.

[16] N. YURCHENKO *et al.: Effect of B2 ordering on the tensile mechanical properties of refractory AlxNb40Ti40V20−x medium-entropy alloys*, Journal of Alloys and Compounds 937 (2023), No. 168465.

[17] S. LAUBE *et al.: Microstructure tailoring of Al-containing compositionally complex alloys by controlling the sequence of precipitation and ordering*, Acta Materialia 218 (2021), No. 117217.

[18] W.-C. HSU *et al.: In situ analysis of the Portevin-Le Chatelier effect from low to high-entropy alloy in equal HfNbTaTiZr system*, Acta Materialia 253 (2023), No. 118981.

[19] A. PORTEVIN; Le Chatelier, F.: *Sur un phénomène observé lors de l'essai de traction d'alliages en cours de transformation*, C. R. Acad. Sci. Paris, 1923, p. 507 – 510, (1923).

[20] P. RODRIGUEZ: *Serrated plastic flow*, Bulletin of Materials Science 6 (1984), p. 653 – 663.

[21] H. CONRAD: *Thermally activated deformation of metals*, JOM 16 (1964), p. 582 – 588.

[22] B. ŠESTÁK; Seeger, Alfred: *Gleitung und Verfestigung in kubisch-raumzentrierten Metallen und Legierungen (I)*, Zeitschrift für Metallkunde 69 (1978), p. 195 – 202.

[23] B. ŠESTÁK; Seeger, Alfred: *Gleitung und Verfestigung in kubisch-raumzentrierten Metallen und Legierungen (II)*, Zeitschrift für Metallkunde 69 (1978), p. 355 – 363.

[24] B. ŠESTÁK; Seeger, Alfred: *Gleitung und Verfestigung in kubisch-raumzentrierten Metallen und Legierungen (III)*, Zeitschrift für Metallkunde 69 (1978), p. 425 – 432.

[25] L. HOLLANG *et al.: Work hardening and flow stress of ultrapure molybdenum single crystals*, Materials Science and Engineering: A 319-321 (2001), p. 233 – 236.

[26] *Metallic materials - Vickers hardness test*, DIN EN ISO 6507-1:2018, DIN Deutsches Institut für Normung e. V. (2018).

[27] J. M. WHEELER *et al.: High temperature nanoindentation: The state of the art and future challenges*, Current Opinion in Solid State and Materials Science 19 (2015), p. 354 – 366.

[28] I.-C. CHOI *et al.: Thermally activated dislocation plasticity in body-centered cubic chromium studied by high-temperature nanoindentation*, Acta Materialia 140 (2017), p. 107 – 115.

[29] D.-H. LEE *et al.: Activation energy for plastic flow in nanocrystalline CoCrFeMnNi high-entropy alloy: A high temperature nanoindentation study*, Scripta Materialia 156 (2018), p. 129 – 133.

[30] W. C. OLIVER; Pharr, G. M.: *An improved technique for determining hardness and elastic modulus using load and displacement sensing indentation experiments*, Journal of Materials Research 7 (1992), p. 1564 – 1583.

[31] W. C. OLIVER; Pharr, G. M.: *Measurement of hardness and elastic modulus by instrumented indentation: Advances in understanding and refinements to methodology*, Journal of Materials Research 19 (2004), p. 3 – 20.

[32] J. M. WHEELER; Michler, J.: *Invited Article: Indenter materials for high temperature nanoindentation*, The Review of scientific instruments 84 (2013), No. 101301.

[33] V. MAIER *et al.: Nanoindentation strain-rate jump tests for determining the local strain-rate sensitivity in nanocrystalline Ni and ultrafine-grained Al*, Journal of Materials Research 26 (2011), p. 1421 – 1430.

[34] D. TABOR: *The hardness of solids*, Review of Physics in Technology 1 (1970), p. 145 – 179.

[35] W. D. NIX; Gao, Huajian: *Indentation size effects in crystalline materials: A law for strain gradient plasticity*, Journal of the Mechanics and Physics of Solids 46 (1998), p. 411 – 425.

[36] H. Warlimont und W. Martienssen, *Springer Handbook of Materials Data,* 2. Ed., Cham, Springer International Publishing, (2018).

[37] H. KHAKUREL *et al.: Machine learning assisted prediction of the Young's modulus of compositionally complex alloys*, Scientific reports, No. 17149.

[38] M. ITO *et al.: Effect of electronegativity on the mechanical properties of metal hydrides with a fluorite structure*, Journal of Alloys and Compounds 426 (2006), p. 67 – 71.

[39] D. WU *et al.: Variation of strain rate sensitivity with grain size in Cr and other body-centred cubic metals*, Journal of Physics D: Applied Physics 47 (2014), No. 175303.

[40] V. MAIER *et al.: Thermally activated deformation processes in body-centered cubic Cr – How microstructure influences strain-rate sensitivity*, Scripta Materialia 106 (2015), p. 42 – 45.

[41] D. S. STONE; Yoder, K. B.: *Division of the hardness of molybdenum into rate-dependent and rate-independent components*, Journal of Materials Research 9 (1994), p. 2524 – 2533.

[42] C. MINNERT *et al.: Thermally activated dislocation mechanism in Mo studied by indentation, compression and impact testing*, Journal of Materials Research 36 (2021), p. 2397 – 2407.

[43] J. ZHAO *et al.: Indentation size and loading strain rate dependent creep deformation of nanocrystalline Mo*, Thin Solid Films 653 (2018), p. 365 – 370.

[44] C. BRANDL *et al.: Temperature-dependent nanoindentation and activation volume in high-purity body-centered cubic chromium*, Materials Science and Engineering: A 852 (2022), No. 143629.

[45] K. IOROI *et al.: Melting Point of Pure Cr and Phase Equilibria in the Cr-Si Binary System*, Journal of Phase Equilibria and Diffusion 43 (2022), p. 229 – 242.

[46] G. K. WHITE; Andrikidis, C.: *Thermal expansion of chromium at high temperature*, Physical review. B, Condensed matter 53 (1996), p. 8145 – 8147.

[47] Q. WEI *et al.: Effect of nanocrystalline and ultrafine grain sizes on the strain rate sensitivity and activation volume: fcc versus bcc metals*, Materials Science and Engineering: A 381 (2004), p. 71 – 79.

[48] M.-S. LEE *et al.: Global and local strain rate sensitivity of commercially pure titanium*, Journal of Alloys and Compounds 803 (2019), p. 711 – 720.

[49] Q.-J. LI *et al.: Strengthening in multi-principal element alloys with local-chemical-order roughened dislocation pathways*, Nature communications, No. 3563.

[50] Y. RAO; Curtin, W. A.: *Analytical models of short-range order in FCC and BCC alloys*, Acta Materialia 226 (2022), No. 117621.

[51] R. ZHANG *et al.: Short-range order and its impact on the CrCoNi medium-entropy alloy*, Nature, p. 283 – 287.

[52] E. ANTILLON *et al.: Chemical short range order strengthening in a model FCC high entropy alloy*, Acta Materialia 190 (2020), p. 29 – 42.

[53] C. BARUFFI *et al.: Screw vs. edge dislocation strengthening in body-centered-cubic high entropy alloys and implications for guided alloy design*, MRS Communications 12 (2022), p. 1111 – 1118.

[54] G. WINKENS *et al.: The influence of lattice misfit on screw and edge dislocation-controlled solid solution strengthening in Mo-Ti alloys*, Communications Materials, 2023, No. 26, (2023). https://www.nature.com/articles/s43246-023-00353-8

[55] A. GHAFAROLLAHI; Curtin, William A.: *Screw-controlled strength of BCC non-dilute and high-entropy alloys*, Acta Materialia 226 (2022), No. 117617.

[56] F. MARESCA; Curtin, William A.: *Theory of screw dislocation strengthening in random BCC alloys from dilute to "High-Entropy" alloys*, Acta Materialia 182 (2020), p. 144 – 162.

[57] J. M. ROSENBERG; Piehler, H. R.: *Calculation of the taylor factor and lattice rotations for bcc metals deforming by pencil glide*, Metallurgical Transactions 2 (1971), p. 257 – 259.

[58] H. CHEN *et al.: Contribution of Lattice Distortion to Solid Solution Strengthening in a Series of Refractory High Entropy Alloys*, Metallurgical and Materials Transactions A 49 (2018), p. 772 – 781.

[59] G. CHIAROTTI: *1.6 Crystal structures and bulk lattice parameters of materials quoted in the volume* in *Zahlenwerte und Funktionen aus Naturwissenschaften und Technik*. Berlin: Springer, (1993), p. 21 – 26.

[60] O. N. SENKOV *et al.: Microstructure and room temperature properties of a high-entropy TaNbHfZrTi alloy*, Journal of Alloys and Compounds 509 (2011), p. 6043 – 6048.

[61] L. VEGARD: *Die Konstitution der Mischkristalle und die Raumfüllung der Atome*, Zeitschrift für Physik 5 (1921), p. 17 – 26.

[62] J. B. NELSON; Riley, D. P.: *An experimental investigation of extrapolation methods in the derivation of accurate unit-cell dimensions of crystals*, Proceedings of the Physical Society 57 (1945), p. 160 – 177.

[63] F. MARESCA; Curtin, William A.: *Mechanistic origin of high strength in refractory BCC high entropy alloys up to 1900K*, Acta Materialia 182 (2020), p. 235 – 249.

[64] R. E. KUBILAY *et al.: High energy barriers for edge dislocation motion in body-centered cubic high entropy alloys*, npj Computational Materials 7 (2021).

[65] D. NGUYEN-MANH *et al.: Self-interstitial atom defects in bcc transition metals: Group-specific trends*, Physical Review B 73 (2006).

[66] A. de VITA; Gillan, M. J.: *The ab initio calculation of defect energetics in aluminium*, Journal of Physics: Condensed Matter 3 (1991), p. 6225 – 6237.

[67] L. DEZERALD *et al.: First-principles prediction of kink-pair activation enthalpy on screw dislocations in bcc transition metals: V, Nb, Ta, Mo, W, and Fe*, Physical Review B 91 (2015).

[68] A. SEEGER; Holzwarth, U.: *Slip planes and kink properties of screw dislocations in high-purity niobium*, Philosophical Magazine 86 (2006), p. 3861 – 3892.

[69] B. YIN *et al.: Yield strength and misfit volumes of NiCoCr and implications for short-range-order*, Nature communications, No. 2507.